# Temperature-dependent structures of proton-conducting Ba(Zr0.8-xCexY0.2)O2.9 ceramics by Raman scattering and x-ray diffraction

Authors: C.-S. Tu, R. R. Chien, V. Hugo Schmidt, S. C. Lee, and C.-C. Huang



C.-S. Tu, R.R. Chien, V.H. Schmidt, S.C. Lee, and C.-C. Huang, “Temperature-dependent structures of proton-conducting Ba(Zr0.8-xCexY0.2)O2.9 ceramics by Raman scattering and x-ray diffraction,” Journal of Physics: Condensed Matter 24, 155403 (6 pp.) (2012), doi: 10.1088/0953-8984/24/15/155403.

# Temperature-dependent structures of proton-conducting $Ba(Zr_{0.8-x}Ce_xY_{0.2})O_{2.9}$ ceramics by Raman scattering and x-ray diffraction

**C-S Tu[1,2], R R Chien[3], V H Schmidt[3], S C Lee[2] and C-C Huang[2]**

[1] Graduate Institute of Applied Science and Engineering, Fu Jen Catholic University, Taipei 24205, Taiwan

[2] Department of Physics, Fu Jen Catholic University, Taipei 24205, Taiwan

[3] Department of Physics, Montana State University, Bozeman, MT 59717, USA

**Abstract**

*In situ* temperature-dependent micro-Raman scattering and x-ray diffraction have been performed to study atomic vibration, lattice parameter and structural transition of proton-conducting $Ba(Zr_{0.8-x}Ce_xY_{0.2})O_{2.9}$ (BZCY) ceramics ($x = 0.0$–$0.8$) synthesized by the glycine–nitrate combustion process. The Raman vibrations have been identified and their frequencies increase with decreasing $x$ as the heavier $Ce^{4+}$ ions are replaced by $Zr^{4+}$ ions. The main Raman vibrations of $Ba(Ce_{0.8}Y_{0.2})O_{2.9}$ appear near 305, 332, 352, 440 and 635 $cm^{-1}$. The X–O (X = Ce, Zr, Y) stretching modes are sensitive to the variation of Ce/Zr ratio. A rhombohedral–cubic structural transition was observed for $x = 0.5$–$0.8$, in which the transition shifts toward higher temperature as cerium increases, except for $Ba(Ce_{0.8}Y_{0.2})O_{2.9}$. A minor monoclinic phase possibly coexists in the rhombohedral matrix for $x = 0.5$–$0.8$. The lower-cerium BZCYs ($x = 0.0$–$0.4$) ceramics do not exhibit any transition in the region of 20–900 °C, indicating a cubic phase at and above room temperature.

(Some figures may appear in colour only in the online journal)

## 1. Introduction

Perovskite-type (Ba, Sr, Ca)(Zr, Ce)$O_3$ oxides exhibit good protonic conduction under hydrogen-containing atmosphere at elevated temperature, and are promising for applications of proton-conducting solid oxide fuel cells (H-SOFCs), hydrogen separation membranes, hydrogen pumps, hydrogen sensors and steam electrolyzers for hydrogen production [1, 2]. For instance, hydrogen-fueled H-SOFCs with BZCY electrolytes made by Yang *et al* [3] achieved a power density of 700 mW $cm^{-2}$ at the relatively low temperature of 700 °C, and BZCY-based cells made by Meng *et al* [4] reached 371 mW $cm^{-2}$. Our group has been investigating thermal stability (in $CO_2$ atmosphere), ionic conductivity and power density in BZCY-based ceramics as functions of cerium/zirconium ratio, glycine–nitrate ratio, sintering parameter and temperature [5–8]. These power densities are competitive with those achieved by O-SOFCs with oxygen-ion-conducting electrolytes. H-SOFCs have two advantages over O-SOFCs, based on the fact that on the anode side there is only hydrogen inflow, with no steam outflow. First, higher fuel utilization can be achieved because there is no loss of fuel flowing out with the steam exhaust gas. Second, anode-supported cells having a relatively thick anode are desirable because the anode has a strong metal framework, and there is much less fuel pressure loss through the anode passages in H-SOFCs because there is no steam counterflow.

Cerate-based proton conductors have a high ionic conductivity but exhibit poor chemical stability in $CO_2$- and $H_2O$-containing atmosphere at elevated temperature [9]. Although zirconate-based proton conductors have lower ionic conductivity, they show good thermal and mechanical stabilities [10]. The previous results suggested that proton-conducting solid solutions between cerate and zirconate may have both high proton conductivity and good chemical stability [11, 12]. $A^{II}B^{IV}O_3$-based proton conductors have been doped in the B site by lower valence elements, typically $Y^{3+}$ ($R^{III} = 0.9$ Å) or trivalent rare earth metal cations, creating oxygen vacancies. Subsequent exposure to humid atmospheres is presumed to lead to the incorporation of protons, resulting in proton conduction [13, 14].

$BaCeO_3$ has a transition sequence of orthorhombic (*Pnma*)–orthorhombic (*Imma*)–rhombohedral ($R\bar{3}c$)–cubic ($Pm\bar{3}m$) at 290, 400 and 900 °C, respectively [15]. Different phases were reported at room temperature for $BaCeO_3$ prepared by various methods, including orthorhombic, tetragonal, pseudocubic and cubic phases [16]. This type of perovskite can crystallize in various structures, depending on processing method and sintering condition. $BaZrO_3$ is cubic at and above room temperature [17]. Yttria-stabilized zirconia (YSZ) has a disordered cubic face-centered fluorite-type lattice in which the $Zr^{4+}$ cations are partially substituted by the $Y^{3+}$ cations and one oxygen vacancy per pair of $Y^{3+}$ ions is generated. The neutron diffraction result suggested a rhombohedral $R\bar{3}c$ phase for $Ba(Ce_{0.8}Y_{0.2})O_{2.9}$ (BCY82) at room temperature [18]. A coexistence of rhombohedral and monoclinic phases was proposed for BCY82 [19].

There is not much knowledge of the temperature-dependent phase diagram regarding the proton-conducting $Ba(Zr, Ce, Y)O_{3-\delta}$ ceramics even though the mixed compounds with the addition of yttrium are important for fuel cell and hydrogen separation membrane applications. The thermal structural property is an important factor for using proton-conducting $Ba(Zr, Ce, Y)O_{3-\delta}$ ceramics in fuel cells. In this work, temperature-dependent x-ray diffraction (XRD) and micro-Raman scattering were employed to investigate atomic vibrations, lattice parameters of the unit cell and structural transitions of $Ba(Zr_{0.8-x}Ce_xY_{0.2})O_{2.9}$ ceramic powders in an argon-containing environment.

## 2. Experimental details

The glycine-to-nitrate (G/N) combustion process was used to synthesize nanosized $Ba(Zr_{0.8-x}Ce_xY_{0.2})O_{2.9}$ (BZCY) ceramic powders as a function of cerium-to-zirconium ratio ($x = 0.0$–$0.8$) [7]. The glycine-to-nitrate molar ratio used to fabricate BZCY powders is G/N = 1/2, because it can fabricate nanosized and single-phase ceramic powders [7]. All synthesized powders were calcined at 1400 °C for 5 h in air. From our previous result [7], the calcined $Ba(Zr_{0.8-x}Ce_xY_{0.2})O_{2.9}$ ceramics ($x = 0.0$–$0.8$) have similar particle sizes of ~35–45 nm, indicating that the size effect in Raman vibration could be ignored.

For *in situ* XRD measurements, a high-temperature Rigaku model MultiFlex x-ray diffractometer with Cu $K\alpha_1$ ($\lambda = 0.154\,06$ nm) and Cu $K\alpha_2$ ($\lambda = 0.154\,44$ nm) radiation was used in the range of 20–900 °C upon heating by steps in an argon-containing atmosphere. The calcined BZCY powders were placed and smoothly pressed on the platinum sample holder. A sum of Gaussian and Lorentzian equations was used to fit XRD spectra for determinations of structures and lattice parameters of the unit cell. For micro-Raman scattering, a double-grating Jobin Yvon model U-1000 double-monochromator with 1800 grooves $mm^{-1}$ gratings and a nitrogen-cooled CCD as a detector were employed. A Coherent model Innova 90 argon laser of wavelength $\lambda =$ 514.5 nm was used as an excitation source and the Raman spectra were collected at 150–1000 $cm^{-1}$ from 20–900 °C by steps.

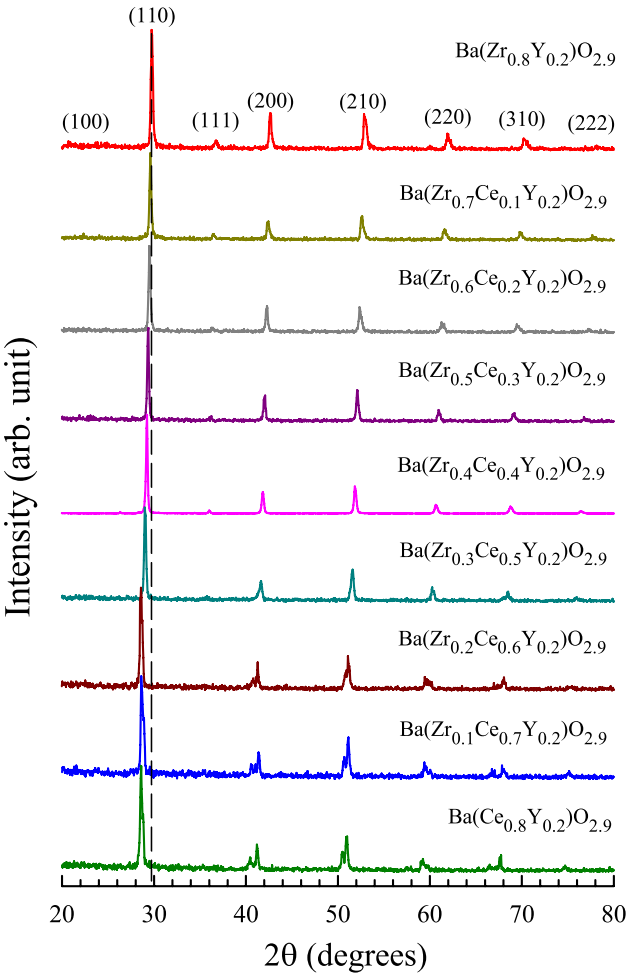


**Figure 1.** X-ray diffraction of BZCY ($x = 0.0$–$0.8$) taken at room temperature. The dashed line is a guide for $2\theta$ shifts.

## 3. Results and discussion

Figure 1 shows the XRD spectra of BZCYs ($x = 0.0$–$0.8$) ceramic powders at room temperature. A second phase was not observed in any of these compounds, indicating that the optimal glycine-to-nitrate process and calcining condition can produce single-phase powders. The main reflection peaks of $Ba(Zr_{0.8}Y_{0.2})O_{2.9}$ (BZY82) include (110), (200), (210), (220) and (310), and weak peaks occur for (100), (111) and (222).

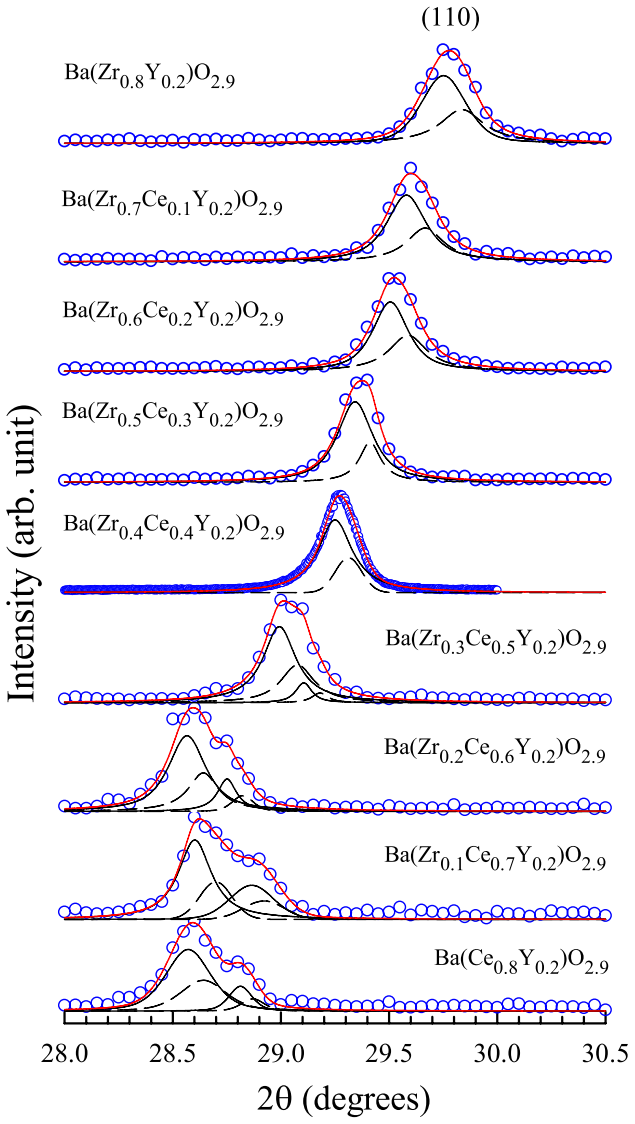


**Figure 2.** The (110) XRD spectra of BZCY ($x = 0.0$–$0.8$) at room temperature. Solid and dashed lines represent reflections from K$\alpha_1$ and K$\alpha_2$ radiation, respectively.

This suggests a simple cubic (sc) unit cell according to the structure-factor calculation [20]. The cubic lattice parameter was estimated from the (110) peak ($2\theta = 29.75°$) and is $a = 4.2436$ Å for BZY82 at room temperature. As indicated by the dashed line, the XRD peak shifts towards lower $2\theta$ degrees as cerium content increases, because $Ce^{4+}$ ($R^{VI} = 0.87$ Å) has a larger ionic radius than $Zr^{4+}$ ($R^{VI} = 0.72$ Å) [21].

Single-peak reflections appear in the XRD spectra of lower-cerium compounds ($x = 0.0$–$0.4$), indicating a cubic phase above room temperature. As cerium increases ($x = 0.5$–$0.8$), the XRD spectra exhibit obvious multi-peak reflections, especially at higher $2\theta$. To study the phase transition development as a function of cerium composition ($x$), the (110) XRD reflections of BZCY ($x = 0.0$–$0.8$) powders taken at room temperature are enlarged in figure 2 with fitting profiles. Solid and dashed lines represent reflections from K$\alpha_1$ and K$\alpha_2$ radiation, respectively. The (110) reflection exhibits an obvious two-peak splitting (from each radiation) for $x = 0.5$–$0.8$, especially a significant shift to

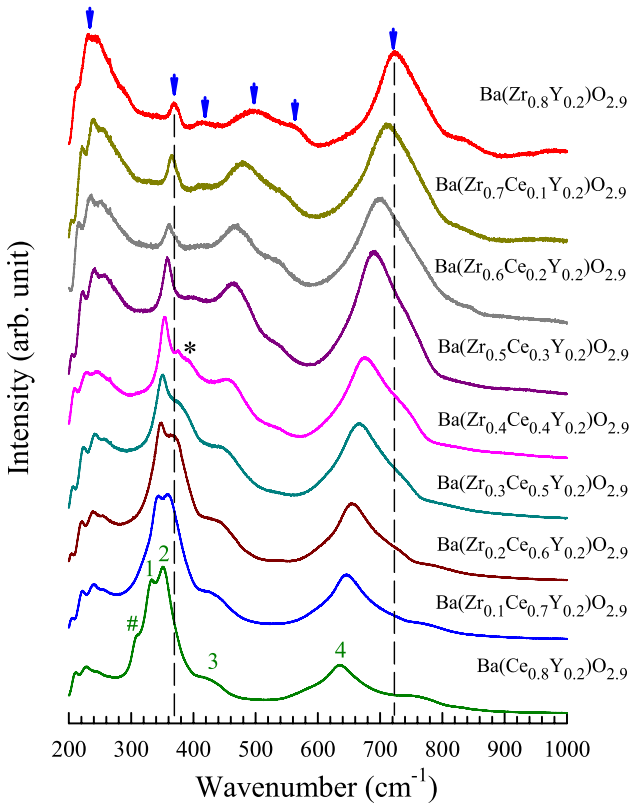


**Figure 3.** Micro-Raman spectra of BZCY ($x = 0.0$–$0.8$) taken at room temperature. The dashed lines are guides for frequency shifts. '1–4' and '#' indicate four major modes and a shoulder vibration in BCY82.

low $2\theta$ angle in $Ba(Zr_{0.2}Ce_{0.6}Y_{0.2})O_{2.9}$. A similar two-peak splitting occurs in (210) and (220) reflections as seen in figure 1 for $x = 0.5$–$0.8$. These two-peak splittings suggest a rhombohedral phase, because two spacings are expected from the (110), (210) and (220) reflections for a rhombohedral unit cell according to the lattice equation;

$$1/d^2 = [(h^2 + k^2 + l^2)\sin^2\alpha + 2(hk + kl + hl) \times (\cos^2\alpha - \cos\alpha)]/[a_R^2(1 - 3\cos^2\alpha + 2\cos^3\alpha)] \quad (1)$$

where $(h, k, l)$ and $(a_R, \alpha)$ are crystallographic orientation and lattice parameters of the rhombohedral unit cell, respectively [20]. In addition, the (200) reflection begins to appear as a two-peak splitting in $Ba(Zr_{0.2}Ce_{0.6}Y_{0.2})O_{2.9}$ as shown in figure 1, implying a development of a minor monoclinic phase in the rhombohedral matrix. According to equation (1), only a single XRD peak is allowed from the (200) reflection for a rhombohedral (R) unit cell. The polar axis of the monoclinic (M) phase is contained in the (110) plane along a direction between that of the tetragonal and rhombohedral polar axes. Additional XRD peaks can occur in the (200) reflection for a monoclinic structure as observed in the monoclinic PZT ceramic [22]. The sudden shift (to low angle) in the (110) reflection of $Ba(Zr_{0.2}Ce_{0.6}Y_{0.2})O_{2.9}$ is likely associated with the appearance of a monoclinic phase. These results suggest that a minor monoclinic phase coexists in the rhombohedral matrix for higher-cerium BZCYs ceramics ($x = 0.5$–$0.8$). This is consistent with the previous

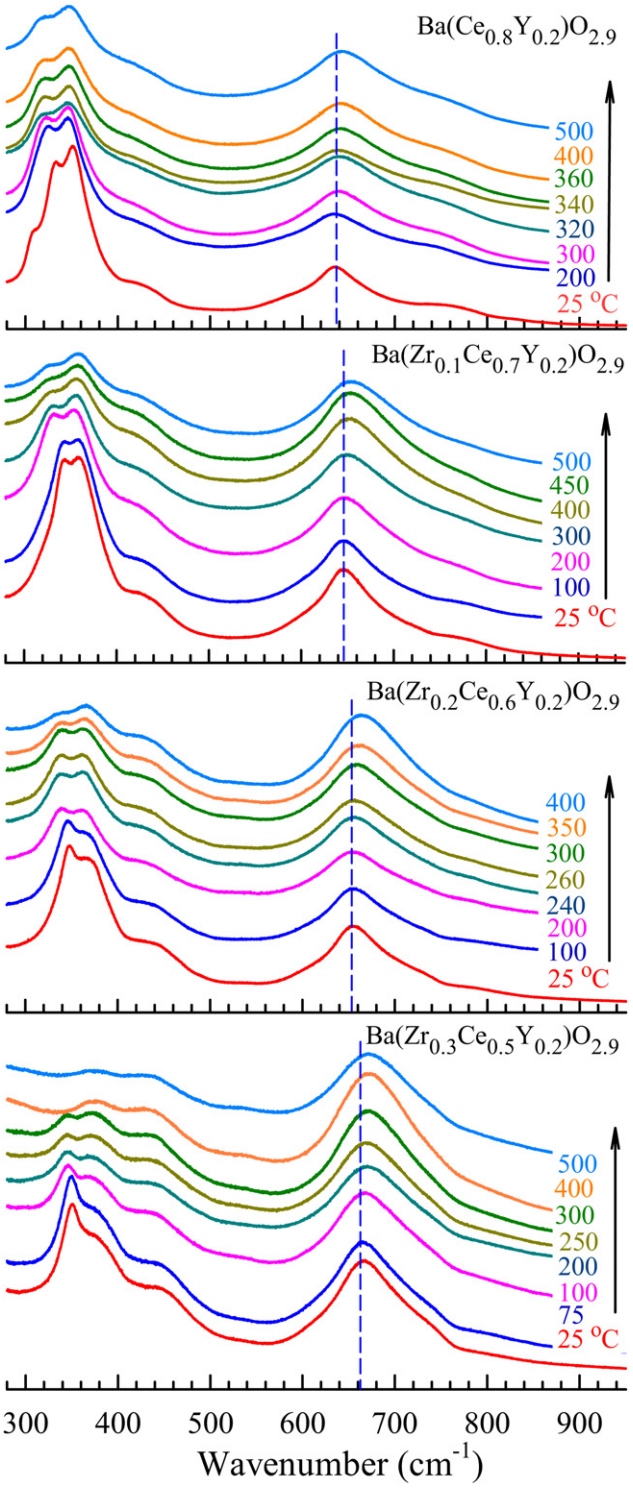


**Figure 4.** *In situ* micro-Raman spectra of BZCY ($x = 0.5$–$0.8$) upon heating. The dashed lines are guides for frequency shifts as temperature increases.

neutron diffraction results, which suggested a coexistence of rhombohedral and monoclinic phases for $Ba(Ce_{0.8}Y_{0.2})O_{2.9}$ (BCY82) at room temperature [19].

Figure 3 shows the micro-Raman spectra of BZCY ($x = 0.0$–$0.8$) ceramic powders at room temperature. The major vibrations of Raman modes of BZY82 appear at ~240, ~370, ~420, ~500, ~560 and ~720 $cm^{-1}$ as indicated by arrows. As indicated by the dashed lines, vibration modes shift towards lower frequency as cerium content increases, due to the larger atomic mass of cerium compared with Zr. As indicated by the '*', a broad Raman mode as a shoulder (beside the 360 $cm^{-1}$ vibration) begins to develop near 380 $cm^{-1}$ in BZCY442 and its intensity grows stronger as cerium increases. The relative intensities of Raman modes near 350 and 380 $cm^{-1}$ become dominant vibrations and are stronger than the Raman mode near 680 $cm^{-1}$ for $x = 0.5$–$0.8$. The occurrence of an extra vibration mode is consistent with the XRD result, in which an obvious multi-peak splitting appears in the higher-cerium BZCY ceramics ($x = 0.5$–$0.8$), due to the reduction in symmetry from a cubic to a rhombohedral phase.

To explain the Raman modes of BCY82, a shoulder vibration ('#') and four major modes ('1–4') are marked in figure 3. Their frequencies are $\nu_{\#} \cong 305$ $cm^{-1}$, $\nu_1 \cong 332$ $cm^{-1}$, $\nu_2 \cong 352$ $cm^{-1}$, $\nu_3 \cong 440$ $cm^{-1}$ and $\nu_4 \cong 635$ $cm^{-1}$. The $BaCeO_3$ rhombohedral $R\bar{3}c$ phase (two formula units per primitive cell) has an irreducible representation as [23]

$$\Gamma = A_{1g}(R) + 4E_g(R) + 3A_{2g}(S) + 2A_{1u}(S) + 3A_{2u}(IR) + 5E_u(IR) + A_{2u}(A) + E_u(A) \quad (2)$$

where (R), (S), (IR) and (A) represent Raman-active, silent, IR-active and acoustic modes, respectively. Three major $E_g$ modes were observed at 104, 322 and 344 $cm^{-1}$ in the $R\bar{3}c$-phase $BaCeO_3$, in which 322 and 344 $cm^{-1}$ correspond to the Ce–O stretching vibrations [23]. $Y_2O_3$ has three major Raman-active vibrations near 302, 332 and 370 $cm^{-1}$, which correspond to the Y–O stretching modes [24]. Thus, the Raman modes of $\nu_1 \cong 332$ $cm^{-1}$ and $\nu_2 \cong 352$ $cm^{-1}$ in BCY82 can be attributed to the Ce–O and Y–O stretching vibrations. The shoulder vibration of $\nu_{\#} \cong 305$ $cm^{-1}$ likely correlates to the 302 $cm^{-1}$ vibration of the Y–O stretching modes [24]. Note that various inter-atomic distances between $Ce^{4+}$ and $O^{2-}$ ions can cause different force constants and vibration frequencies. As shown in figure 3, $\nu_1$ and $\nu_2$ increase with decreasing $x$ as the heavier $Ce^{4+}$ ions are replaced by $Zr^{4+}$ ions. The Raman modes of $\nu_1$ and $\nu_2$ merge into a single mode for $x = 0.0$–$0.3$ due to the increase of symmetry from the rhombohedral to the cubic phase. This result reveals that the Raman modes associated with the X–O (X = Ce, Zr, Y) stretching modes in the region of 330–380 $cm^{-1}$ are sensitive to the change of cerium content in the BZCY system.

The weak and broad Raman mode of $\nu_3 \cong 440$ $cm^{-1}$ does not occur in the $R\bar{3}c$-phase $BaCeO_3$. A single Raman vibration of ~461 $cm^{-1}$ was observed in the fluorite structure $CeO_2$ and corresponds to the $F_{2g}$ Raman-active triply degenerate mode [25]. This mode is the symmetrically radial breathing mode of the $CeO_8$ vibration unit [26]. The Raman spectrum of $CeO_2$–$ZrO_2$ ceramic also exhibits a strong vibration near 470 $cm^{-1}$ due to the $F_{2g}$ mode of the fluorite-type lattice [27]. Thus, the weak Raman vibration of $\nu_3 \cong 440$ $cm^{-1}$ in BCY82 can be viewed as a symmetric radial breathing mode of the six oxygen ions around $Ce^{4+}$ and $Y^{3+}$ ions in the perovskite structure, in which the frequency increases with decreasing $x$ as the heavier $Ce^{4+}$ ions are replaced by $Zr^{4+}$ ions.

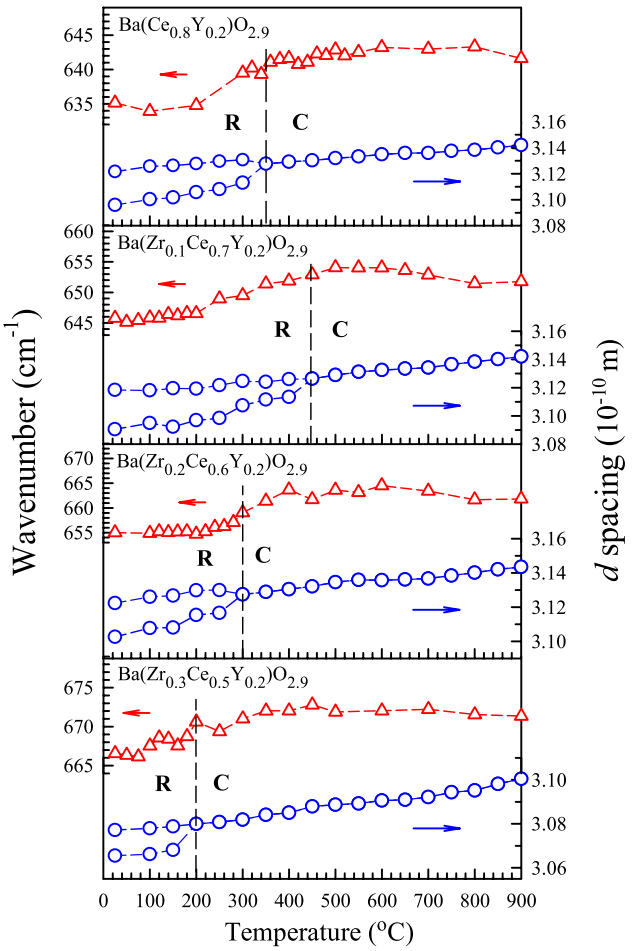


**Figure 5.** Temperature-dependent Raman vibration (near 630–730 $cm^{-1}$) and $d$ spacing calculated from the (110) XRD reflections of BZCY ($x = 0.5$–$0.8$) upon heating. The dashed lines indicate the R–C transition temperatures.

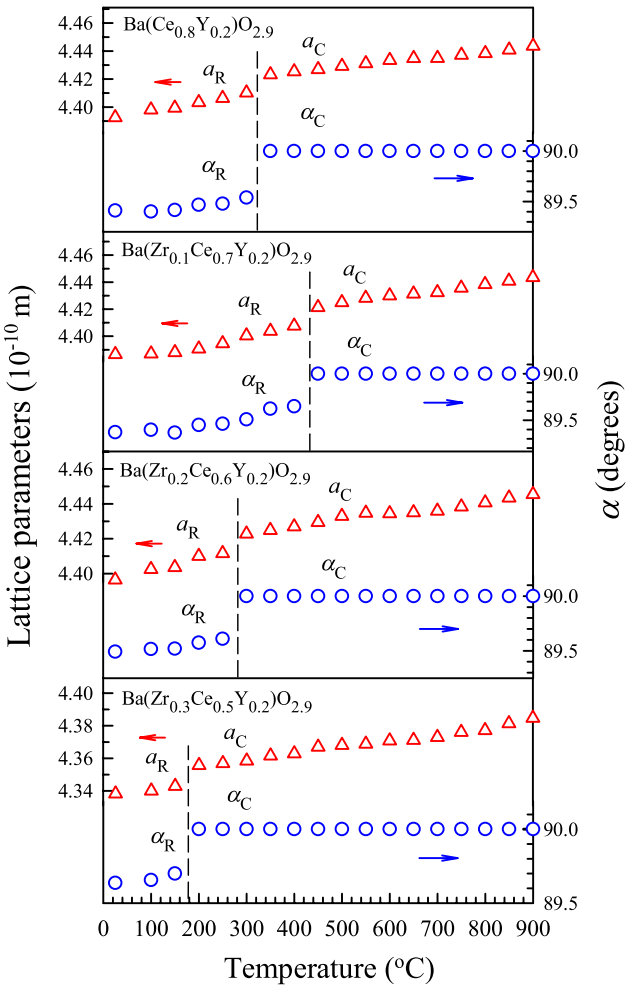


**Figure 6.** Temperature-dependent lattice parameters calculated from the (110) XRD reflections of BZCY ($x = 0.5$–$0.8$) upon heating. The dashed lines indicate the R–C transition temperatures.

A strong and broad Raman vibration appears in the region of 620–650 $cm^{-1}$ in $Y_2O_3$–$ZrO_2$, $CeO_2$–$ZrO_2$ [28, 29] and $Zr_{1-x}Y_xO_{2-x/2}$ [30]. The 640 $cm^{-1}$ vibration in the 3% (mole fraction) $Y_2O_3$–$ZrO_2$ was attributed to the Zr–O stretching mode with $Zr^{4+}$ and $O^{2-}$ ions vibrate along the $z$ axis in the structure of tetragonal-phase $ZrO_2$ [31]. Thus, the $v_4 \cong$ 635 $cm^{-1}$ of BCY82 in figure 3 should correspond to the Ce–O stretching mode. The $v_4$ shifts to higher frequency with decreasing $x$ as the heavier $Ce^{4+}$ ions are replaced by $Zr^{4+}$ ions.

To illustrate the evolution of Raman spectra as temperature increases, *in situ* temperature-dependent micro-Raman spectra are given in figure 4 for BZCY ($x =$ 0.5–0.8) upon heating. As indicated by the dashed lines, the Raman modes near 640–660 $cm^{-1}$ shift to higher frequencies as temperature increases. The double peaks near 340–370 $cm^{-1}$ become broader and their relative intensities decrease gradually as temperature increases.

Figure 5 shows temperature-dependent Raman vibrations near 630–730 $cm^{-1}$ and $d$ spacings of BZCY ceramic powders for the higher-cerium compounds ($x = 0.5$–$0.8$) upon heating. The $d$ spacing calculated from the (110) XRD peak and $2\theta$ reflection obey the Bragg law, $2d_{hkl} \sin\theta_{hkl} = n\lambda$. The Raman vibration mode (near 630–730 $cm^{-1}$) exhibits a step-up-like increase in frequency as temperature approaches the structural transition, while two $d$ spacings from the (110) reflection merge into a single $d$ spacing of the cubic phase. For $Ba(Zr_{0.3}Ce_{0.5}Y_{0.2})O_{2.9}$, the rhombohedral (R)–cubic (C) transition takes place near 200 °C upon heating. This transition shifts toward higher temperature as cerium content increases, except for BCY82.

Figure 6 shows temperature-dependent lattice parameters ($a$ and $\alpha$) of the rhombohedral and cubic phases of higher-cerium BZCY ($x = 0.5$–$0.8$) upon heating. The lattice parameters of the unit cell were determined by fitting the (110) reflection, which is the most pronounced peak. The lattice parameters exhibit a step-up-like anomaly as temperature approaches the transition temperature as indicated by the dashed line. The gradual increase of lattice parameters ($a_R$ and $a_C$) is mainly due to thermal expansion of the unit cell. Results for lower-cerium BZCY ($x = 0.0$–$0.4$) ceramic powders are not shown because they have no obvious phase transition above room temperature.

The phase diagram (transition temperature versus Ce content) of BZCY ($x = 0.0$–$0.8$) ceramics upon the heating process is summarized in figure 7. A rhombohedral (R)–cubic

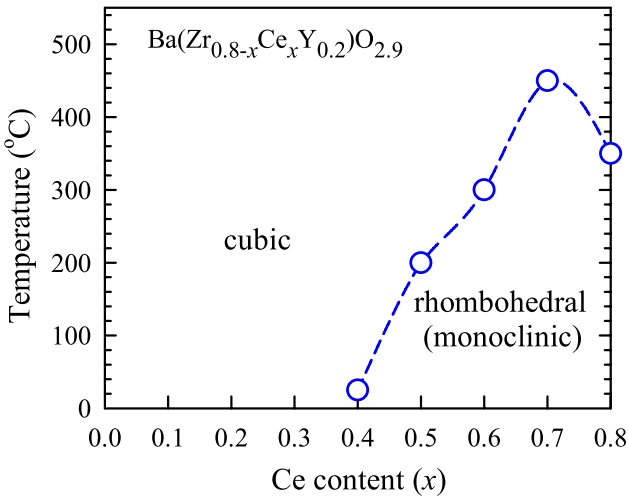


**Figure 7.** Phase diagram (transition temperature versus Ce content) of calcined BZCY ($x = 0.0$–$0.8$) ceramic powders. The dashed line is the estimated phase boundary. Rhombohedral (monoclinic) represents a minor monoclinic phase coexists in the rhombohedral matrix.

(C) phase transition occurs in higher-cerium BZCY ceramics for $x = 0.5$–$0.8$. In addition, a minor monoclinic phase coexists in the rhombohedral matrix for $x = 0.5$–$0.8$. The R–C transition temperature increases with increasing Ce content, except that the transition of BCY82 occurs at lower temperature than $Ba(Zr_{0.1}Ce_{0.7}Y_{0.2})O_{2.9}$. This may imply that the R phase is favored both by Ce replacing Zr, and by Ce–Zr disorder on the perovskite B sites.

## 4. Conclusions

*In situ* temperature-dependent micro-Raman scattering and XRD have been used to investigate structures, lattice parameters, Raman vibration modes and phase transitions of calcined BZCY ceramics ($x = 0.0$–$0.8$) synthesized by the glycine–nitrate combustion process with G/N = 1/2. A second phase (other than perovskite) was not observed for BZCY ceramic powders calcined at 1400 °C for 5 h. A rhombohedral–cubic transition was observed in higher-cerium BZCYs ($x = 0.5$–$0.8$) and the transition shifts towards higher temperature as cerium content increases, except for BCY82. A minor monoclinic phase coexists in the rhombohedral matrix in the higher-cerium BZCYs ($x = 0.5$–$0.8$). The lower-cerium BZCY ceramics ($x = 0.0$–$0.4$) have only a cubic phase at and above room temperature. The X–O (X = Ce, Zr, Y) stretching modes are sensitive to the change of cerium content and can be used to study the doping or substitution effects of the electrical conductivity and electrochemical properties in proton-conducting BZCY ceramics. This work reveals that the lower-cerium BZCY ($x = 0.0$–$0.4$) ceramics exhibit thermal structural stability in the high-temperature region and are promising for applications of proton-conducting solid oxide fuel cells.

## Acknowledgments

The authors would like to thank Dr J Liang (Fu Jen Catholic University) for the Raman scattering apparatus. This work was supported by the DOE under subcontract DE-AC06-76RL01830 from Battelle Memorial Institute and PNNL, and by the National Science Council of Taiwan grant nos. 96-2112-M-030-001 and 100-2112-M-030-002-MY3.

## References

[1] Iwahara H, Uchida H, Kondo K and Ogaki K 1988 *J. Electrochem. Soc.* **135** 529
[2] Iwahara H 1995 *Solid State Ion.* **77** 289
[3] Yang L, Zuo C, Wang S, Cheng Z and Liu M 2008 *Adv. Mater.* **20** 3280
[4] Meng G, Ma G, Ma Q, Peng R and Liu X 2007 *Solid State Ion.* **178** 697
[5] Tu C S, Chien R R, Schmidt V H, Lee S C, Huang C C and Tsai C L 2009 *J. Appl. Phys.* **105** 103504
[6] Tsai C L, Kopczyk M, Smith R J and Schmidt V H 2010 *Solid State Ion.* **181** 1083
[7] Chien R R, Tu C S, Schmidt V H, Lee S C and Huang C C 2010 *Solid State Ion.* **181** 1251
[8] Tu C S, Huang C C, Lee S C, Chien R R, Schmidt V H and Tsai C L 2010 *Solid State Ion.* **181** 1654
[9] Tanner C W and Virkar A V 1996 *J. Electrochem. Soc.* **143** 1386
[10] Kreuer K D 1997 *Solid State Ion.* **97** 1
[11] Zuo C, Zha S, Liu M, Hatano M and Uchiyama M 2006 *Adv. Mater.* **18** 3318
[12] Zhong Z 2007 *Solid State Ion.* **178** 213
[13] Norby T, Widerøe M, Glöckner R and Larring Y 2004 *Dalton Trans.* **19** 3012
[14] Kreuer K D 2003 *Annu. Rev. Mater. Res.* **33** 333
[15] Knight K S 2001 *Solid State Ion.* **145** 275
[16] Melekh B T, Egorov V M, Baikov Y M, Kartenko N F, Filin Y N, Kompan M E, Novak I I, Venus G B and Kulik V B 1997 *Solid State Ion.* **97** 465
[17] Charrier-Cougoulic I, Pagnier T and Lucazeau G 1999 *J. Solid State Chem.* **142** 220
[18] Takeuchi K, Loong C K, Richardson J W, Guanb J, Dorris S E and Balachandran U 2000 *Solid State Ion.* **138** 63
[19] Loong C K, Ozawa M, Takeuchi K, Ui K and Koura K 2006 *J. Alloys Compounds* **408–412** 1065
[20] Cullity B D 1978 *Elements of X-ray Diffraction* (Reading, MA: Addison-Wesley)
[21] Shannon R D 1976 *Acta Crystallogr.* A **32** 751
[22] Guo R, Cross L E, Park S E, Noheda B, Cox D E and Shirane G 2000 *Phys. Rev. Lett.* **84** 5423
[23] Gupta H C, Simon P, Pagneir T and Lucazeau G 2001 *J. Raman Spectrosc.* **32** 331
[24] Nigara Y, Ishigame M and Sakura T 1971 *J. Phys. Soc. Japan* **30** 453
[25] Long R Q, Huang Y P and Wan H L 1997 *J. Raman Spectrosc.* **28** 29
[26] Kosacki I, Suzuki T, Anderson H U and Colomban P 2002 *Solid State Ion.* **149** 99
[27] Reddy B M, Khan A, Lakshmanan P, Aouine M, Loridant S and Volta J C 2005 *J. Phys. Chem.* B **109** 3355
[28] Ma S Z, Liao F H, Li S X, Xu M Y, Li J R, Zhang S H, Chen S M, Huang R L and Gao S 2003 *J. Mater. Chem.* **13** 3096
[29] Hattori M, Takeda Y, Lee J H, Ohara S, Mukai K, Fukui T, Takahashi S, Sakaki Y and Nakanishi A 2004 *J. Power Sources* **131** 247
[30] Yashima M, Ohtake K, Arashi H, Kakihana M and Yoshimura M 1993 *J. Appl. Phys.* **74** 7603
[31] Tang X and Zheng X 2004 *J. Mater. Sci. Technol.* **20** 485